1 NARROW LINE REGION PROPERTIES

1.1 INTRODUCTION

X-ray and UV spectroscopy has revealed high-velocity outflows to be nearly ubiquitous in high accretion rate quasars. Strong evidence for high-velocity outflows include BALs, NALs and blueshifts in high-ionisation broad emission-lines. This suggests that the energy released by quasars can have a dramatic effect on their immediate environment.

The BH mass and the mass of the host galaxy spheroid are strongly correlated. This suggests that the BH and bulge grown synchronously, with the energetic output of the rapidly-accreting BH coupling with the gas in the host galaxy and regulating star formation and the growth of the BH itself (e.g. Silk and Rees, 1998; King, 2003; Di Matteo, Springel, and Hernquist, 2005; King and Pounds, 2015). If this picture is true, then quasars should be capable of driving powerful outflows over galactic scales. In recent years, a huge amount of resources have been devoted to searching for observational evidence of these galaxy-wide, quasar-driven outflows. This has resulted in recent detections of outflows in quasar-host galaxies using tracers of atomic, molecular, and ionised gas (e.g. Nesvadba et al., 2006; Arav et al., 2008; Nesvadba et al., 2008; Moe et al., 2009; Dunn et al., 2010; Alexander et al., 2010; Harrison et al., 2012; Harrison et al., 2014; Nesvadba et al., 2010; Rupke and Veilleux, 2013; Veilleux et al., 2013; Nardini et al., 2015; Feruglio et al., 2010; Alatalo et al., 2011; Cimatti et al., 2013; Cicone et al., 2014).

One particularly successful technique has been using forbidden emission-lines to probe conditions in the AGN NLR. Because of its high equivalent width, [O III]$\lambda\lambda$4960,5008 is the most studied of the narrow AGN emission-lines. The [O III] emission is found to consist of two distinct components: a narrow, 'core' component, with a velocity close to the systemic redshift of the host galaxy, and a broader 'wing' component, which is normally blueshifted. The general consensus is that the core component is dominated by the gravitational potential of the host galaxy whereas the broad, blueshifted wing traces outflowing gas. The relative balance between the core and wing

components varies significantly from object to object, and may depend on properties of the AGN (e.g. luminosity; Shen and Ho, 2014).

Observations of broad velocity-widths and blueshifts in narrow emission-lines stretch back several decades (e.g. Weedman, 1970; Stockton, 1976; Heckman et al., 1981; Veron, 1981; Feldman et al., 1982; Heckman, Miley, and Green, 1984; Vrtilek, 1985; Whittle, 1985; Boroson and Green, 1992). However, these studies rely on small samples, which are often unrepresentative of the properties of the AGN population. More recently, the advent of large optical spectroscopic surveys (e.g. SDSS) have facilitated studies of the NLR in tens of thousands of AGN (e.g. Boroson, 2005; Greene and Ho, 2005; Zhang et al., 2011; Mullaney et al., 2013; Zakamska and Greene, 2014; Shen and Ho, 2014). This has provided constraints on the prevalence and drivers of ionised outflows. At the same time, there is strong evidence from spatially resolved spectroscopic observations that these outflows are extended over galaxy scales (e.g. Greene et al., 2009; Greene et al., 2011; Hainline et al., 2013; Harrison et al., 2012; Harrison et al., 2014).

However, these studies do not cover the redshift range when star formation and BH accretion peaked ($2 \lesssim z \lesssim 4$), which is when quasar feedback is predicted to be at its most effective. At these redshifts bright optical emission-lines including the [O III] doublet are redshifted to near-infrared wavelengths, where observations are much more challenging. As a consequence, studies at high redshifts have typically relied on relatively small numbers of objects (e.g. Netzer et al., 2004; Sulentic et al., 2004; Shen, 2016). These studies find [O III] to be broader in more luminous AGN, suggesting that AGN efficiency in driving galaxy-wide outflows increases with luminosity (e.g. Netzer et al., 2004; Nesvadba et al., 2008; Kim et al., 2013; Brusa et al., 2015; Carniani et al., 2015; Perna et al., 2015; Bischetti et al., 2016). The fraction of objects with very weak [O III] emission also appears to increase with redshift and/or luminosity (e.g. Netzer et al., 2004).

Other recent studies have looked at the [O III] emission properties of extreme objects - e.g. heavily obscured quasars (Zakamska et al., 2016) and the most luminous quasars (Bischetti et al., 2016) - at redshifts $z \sim 2$. When detected, the [O III] emission in these objects is extremely broad and strongly blueshifted. These observations are consistent with galaxy formation mod-

Table 1.1: The numbers of quasars with [O III] line measurements and the spectrographs and telescopes used to obtain the near-infrared spectra.

Spectrograph	Telescope	Number
FIRE	MAGELLAN	31
GNIRS	GEMINI-N	28
ISAAC	VLT	7
LIRIS	WHT	7
NIRI	GEMINI-N	29
NIRSPEC	Keck II	3
SINFONI	VLT	80
SOFI	NTT	76
TRIPLESPEC	ARC-3.5m	27
TRIPLESPEC	P200	45
XSHOOTER	VLT	21
Total		354

els that predict AGN feedback to be strongest in luminous, dust-obscured quasars.

In this chapter we analyse the [O III] properties of a sample of 354 high-luminosity, redshift $1.5 < z < 4$ quasars. To date, this is the largest study of the NLR properties of high redshift quasars.

1.2 QUASAR SAMPLE

From our near-infrared spectroscopic catalogue (Chapter **??**), we have selected 354 quasars which have spectra covering the strong, narrow [O III] doublet. The broad Balmer Hβ line has also been observed for all but two of the sample. For 165 quasars, the spectra extend to the broad Hα emission-line at 6565Å, and in 260 objects optical spectra, including C IV, are also available (mostly from SDSS/BOSS). The sample covers a wide range in redshifts ($1.5 \lesssim z \lesssim 4$) and luminosities ($45.5 \lesssim \log L_{Bol} \lesssim 49$ erg s^{-1}). The spectrographs and telescopes used to obtain the near-infrared spectra are summarised in Table 1.1.

In this section, we describe how emission-line parameters are derived. Our approach is to model the spectra using a power-law continuum, an empirical Fe II template (taken from Boroson and Green 1992) and multiple Gaussian components to model the emission from the broad and narrow emission-line regions. Non-parametric properties are then derived from the best-fitting model. This approach, which is commonly adopted in the literature (e.g. Shen et al., 2011; Shen and Liu, 2012; Shen, 2016), is more robust when analysing spectra with limited S/N (in comparison to measuring line properties directly from the data) and allows different emission-lines to be de-blended.

The same approach was used to model the Hβ/[O III] complex in Chapter **??**. However, a number of small adjustments have been made to the model (Section 1.3.3). Hα emission-line properties (used to estimate the quasar systemic redshift) are also re-derived in this Chapter using a slightly modified model (Section 1.3.5) to the one adopted in Chapter **??**. C IV emission-line properties (used to infer the strength of BLR outflows) are taken directly from Chapter **??**.

1.3.1 *Transforming spectra to the quasar rest-frame*

Before a spectrum can be modelled, it must first be transformed to the quasar rest-frame. The redshift used in this transformation is either derived from the peak of the broad Hα emission (~ 40 per cent of our sample), from the peak of the broad Hβ emission (~ 40 per cent) or from the peak of the narrow [O III] emission (20 per cent). The rest-frame transformation is only required to be accurate to within ~1000 $\mathrm{km\,s^{-1}}$of the systemic redshift for our fitting procedure to work. In later sections, more precise estimates of the systemic redshift will be calculated using our parametric model fits.

1.3.2 *Removing Fe II emission*

Fe II emission is generally strong in the vicinity of Hβ/[O III]. Therefore, before Hβ/[O III] is modelled, we first model and subtract the continuum and Fe II emission using the procedure described in Chapter **??**.

We encountered 24 objects for which Fe II emission appears to be present in the spectrum even after the subtraction proce-

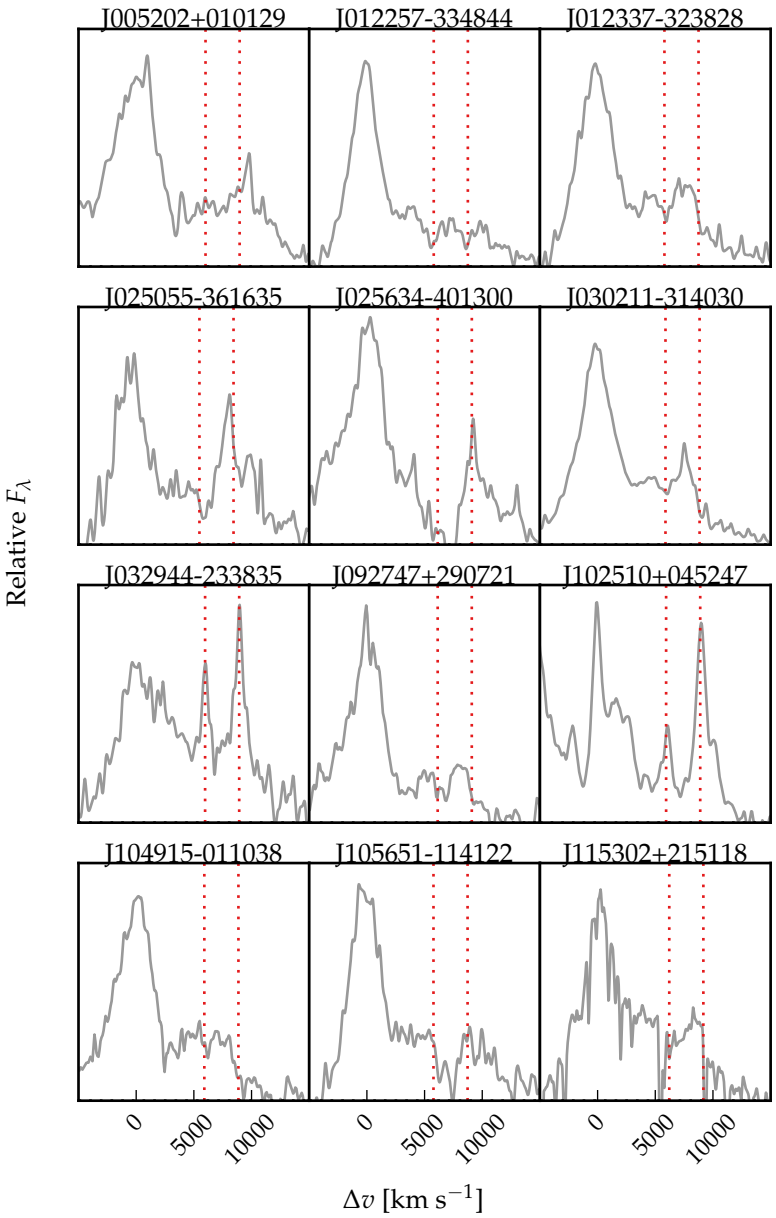

Figure 1.1: Spectra of the 24 objects for which significant Fe II emission is still visible following our Fe II-subtraction procedure. Spectra have been smoothed via convolution with a 100 km s^{-1} Gaussian kernel. The vertical lines indicate the expected positions of the [O III] doublet (which is generally very weak) with the systemic redshift defined using the peak of the broad Hβ emission.

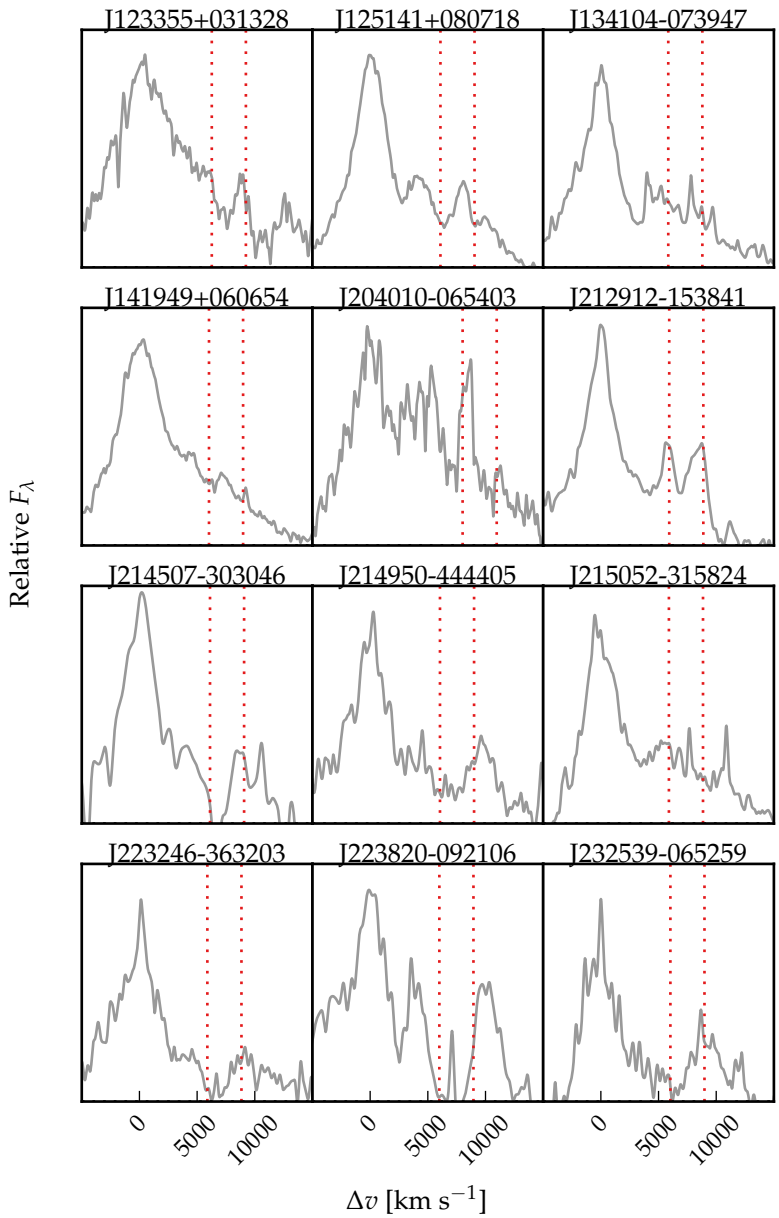

Figure 1.1: Continued.

Table 1.2: Summary of models used to fit the Hβ emission, and the number of quasars each model is applied to.

Model	Fix centroids?	Number
2 broad Gaussians + 1 narrow Gaussian	No	9
2 broad Gaussians	No	274
2 broad Gaussians	Yes	39
1 broad Gaussian	N/A	8

dure (Figure **??**). In these objects the relative strengths of the Fe II lines differ significantly from those of I Zw 1, on which the Boroson and Green, (1992) Fe II template we use is based. The residual Fe II emission is at rest-frame wavelengths very close to zero-velocity wavelengths of the [O III] doublet, which is generally very weak in these objects. The Gaussians we fit to the spectra to model [O III] are therefore strongly biased, and the [O III] emission properties we infer from the model are in error by large factors.

For example, J223819-092106 was analysed by Shen, (2016) using a very similar model. Shen, (2016) reported the [O III] emission in this object to be shifted by $\sim$ 7500 km s^{-1}relative to the Hewett and Wild, (2010) systemic redshift. Our analysis suggests that emission which was modelled by Shen, (2016) as [O III] is more likely to be poorly-subtracted Fe II emission. Because the derived [O III] emission properties can be strongly biased in objects so-affected, these objects are flagged and are excluded from our analysis in the remainder of this Chapter (leaving 330 objects in our sample).

1.3.3 *Modelling Hβ/[O III]*

The Hβ and [O III] emission is fit using a similar procedure to the one described in Chapter **??**. However, we make a number of modifications to the parametric model employed, which we will now describe.

Hβ

In general, Hβ is modelled by two Gaussians with non-negative amplitudes and FWHM greater than 1200 km s^{-1}. In 10 objects Hβ is modelled with a single Gaussian and in 41 objects Hβ is modelled with two Gaussians, but the velocity centroids of the two Gaussians are constrained to be equal. These spectra gen-

erally have low S/N, and adding extra freedom to the model does not significantly decrease the reduced χ^2. In addition there are cases where the blue wing of the Hβ emission is below the lower wavelength limit of the spectra; in these cases models with more freedom are insufficiently constrained by the data.

Contributions to the Hβ emission from the NLR is weak in the vast majority of our sample, and in general we do not include an additional Gaussian component to model this emission. In nine objects features in the model - data residuals suggest that a narrow emission component is significant, and an additional narrow Gaussian is included for these quasars. It is likely that there is some not insignificant contribution from the NLR in other quasars in our sample. If this is the case then measures of the Hβ velocity width will be biased to lower values on average. However, our systemic redshift estimates that use the peak of the Hβ emission (Section 1.3.10) will not be affected. The Hβ models, and the numbers of quasars each model is applied to, are summarised in Table 1.2.

[O III]

Each component of the [O III] doublet is fit with one or two Gaussians, depending on the fractional reduced χ^2 difference between the one- and two-component models. Concretely, if the addition of the second Gaussian decreases the reduced χ^2 by more than 5 per cent then the double-Gaussian model is accepted. One hundred and twenty-eight spectra are fit with a single Gaussian and 140 with two Gaussians. The peak flux ratio of the [O III] 4960 Å and 5008Å components are fixed at the expected 1:3 ratio and the width and velocity offsets are set to be equal[1].

In 62 objects with very weak [O III] (mean EQW~ 2Å) we found that the Gaussian model has a tendency to fit features to the noise. In some cases this can lead to large errors on the [O III] line properties. To avoid this problem, we instead fit a fixed [O III] template to the spectra, with the overall scaling the only free-parameter in the fit. This template is generated by running our line-fitting routine on a median composite spectrum of the 268 quasars with [O III] line measurements. The spectra used to construct the composite were first de-redshifted and

1 For J003136+003421, a significantly better fit ($\Delta\chi^2_\nu \sim 25\%$) is obtained when the peak flux ratio constraint relaxed; the peak ratio of the best-fitting model is 1:2.13.

Table 1.3: Summary of models used to fit the [O III] emission, and the number of quasars each model is applied to.

Model	Number
2 Gaussians	140
1 Gaussian	128
Template	62

continuum- and Fe II-subtracted. The [O III] models, and the numbers of quasars each model is applied to, are summarised in Table 1.3.

In Figure 1.2 we show example fits to 15 objects, chosen at random. The mean reduced chi-squared value is 1.74 and, in general, there are no strong features observable in the spectrum minus model residuals.

Comment on why chi-squared is so big

1.3.4 *Deriving upper limits on the [O III] EQW*

Firstly, the best-fitting model comprising the continuum, Fe II, and Hβ emission is subtracted from the spectra, leaving behind only emission due to [O III]. These spectra are then convolved with a Gaussian (width 200 km s^{-1}) in order to estimate the noise-free flux. From each of these spectra we generate 100 mock spectra, with the flux at each wavelength randomly drawn from a Normal distribution with a mean equal to the smoothed flux and a width equal to the error on the flux. We then perform an error-weighted linear least-squares regression with the [O III] template described in the preceding section. The EQW and its error are then defined as the mean and root-mean-square error of the best-fitting EQW in the 100 realisations. We define the upper limit on the [O III] EQW as the mean plus the error.

Paul: does this way of deriving upper limits make sense? This negelects the uncertainty on the fit to the continuum/iron/other emission. Just use the uncertainty from my parameter uncertainties, but be careful with whether I am using template or not. Then use upper limit if the EQW < 3sigma (say)

1.3.5 *Modelling Hα*

There are 217 quasars in our sample with spectra covering the Hα emission-line. Below, we use the peak of the Hα emission as one estimate of the quasar systemic redshift. In this section we describe how the Hα emission was modelled.

The continuum emission is first modeled and subtracted using the procedure described in Chapter **??**. We then test five different models with increasing degrees of freedom to model the Hα emission. The models are summarised in Table 1.4. They

Table 1.4: Summary of models used to fit the Hα emission, and the number of quasars each model is applied to.

Model	Components	Fix centroids?	Number
1	1 broad Gaussian	N/A	10
2	2 broad Gaussians	Yes	71
3	2 broad Gaussians	No	32
4	2 broad Gaussians + narrow Gaussians	Yes	51
5	2 broad Gaussians + narrow Gaussians	No	53

are (1) a single broad Gaussian; (2) two broad Gaussians with identical velocity centroids; (3) two broad Gaussians with different velocity centroids; (4) two broad Gaussians with identical velocity centroids, and additional narrower Gaussians to model narrow Hα emission, and the narrow components of [N II]$\lambda\lambda$6548,6584 and [S II]$\lambda\lambda$6717,6731; (5) two broad Gaussians with different velocity centroids, and additional narrower Gaussians. If used, the width and velocity of all narrow components are set to be equal in the fit, and the relative flux ratio of the two [N II] components is fixed at the expected value of 2.96.

In order to determine which model is selected for each spectrum, we use the following procedure. Each of the five models are fit to every spectrum and the reduced-χ^2 recorded. Initially, the model with the smallest reduced-χ^2 is selected. We then measure how the reduced-χ^2 changes as the complexity of the model is decreased (i.e. considering the models in Table 1.4 in descending order). If the reduced-χ^2 changes by less than ten per cent, then the simpler model is selected.

1.3.6 *Derived parameters*

All [O III] line properties are derived from the [O III]λ5008 emission, but, as described above, the kinematics of [O III]λ4960 are constrained by our fitting routine to be identical.

We do not attach any physical meaning to the individual Gaussian components used in the model. Decomposing the [O III] emission into a narrow component component at the systemic redshift and a lower-amplitude, blueshifted broad component is subject to large uncertainties and is highly dependent on the spectral S/N and resolution. Furthermore, there is no theoretical justification that the broad component should have a Gaussian profile.

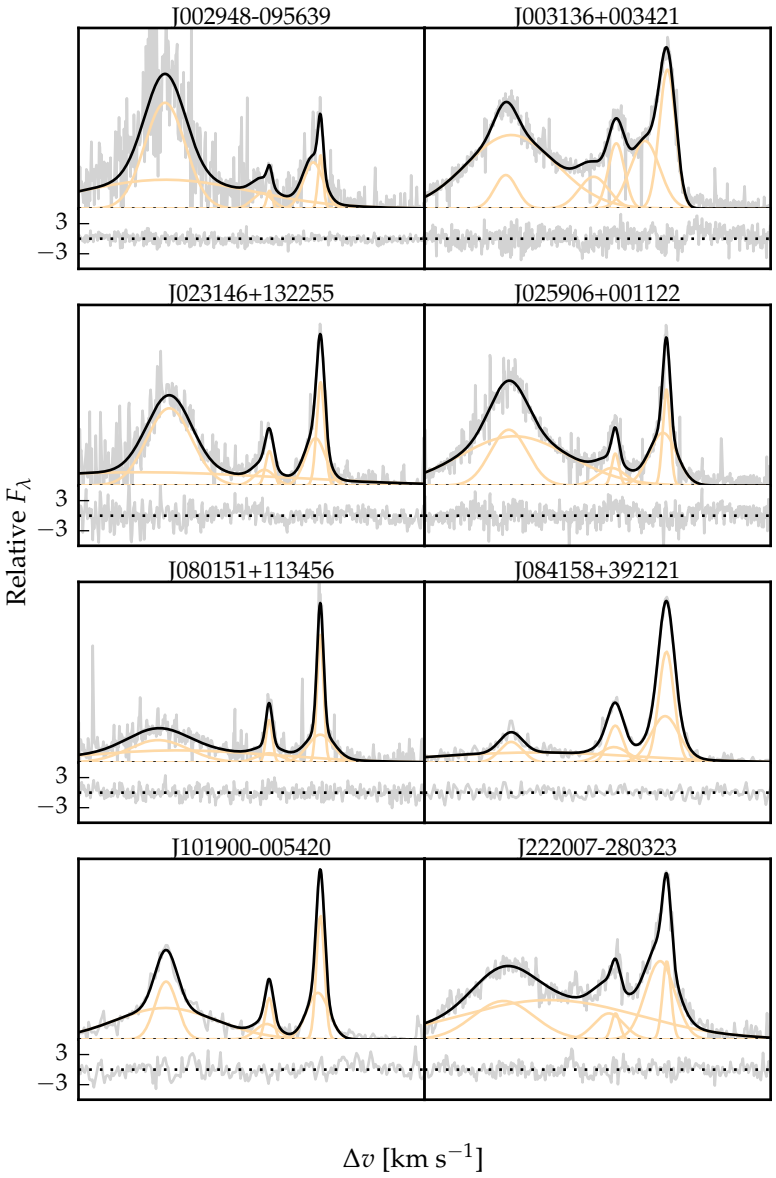

Figure 1.2: Model fits to the continuum- and Fe II-subtracted Hβ/[O III] emission in 15 quasars, chosen at random. The data is shown in grey, the best-fitting model in black, and the individual model components in orange. The peak of the [O III] emission is used to set the redshift, and Δv is the velocity shift from the rest-frame transition wavelength of Hβ . Below each spectrum we plot the data minus model residuals, scaled by the errors on the fluxes.

Table 1.5: The format of the table containing the emission-line properties from our parametric model fits.

Column	Name	Units	Description
1	UID		Catalogue name
2	OIII_V5	$\mathrm{km\,s^{-1}}$	[O III] v_5
3	OIII_V5_ERR	$\mathrm{km\,s^{-1}}$	Uncertainty in v_5
4	OIII_V10	$\mathrm{km\,s^{-1}}$	[O III] v_{10}
5	OIII_V10_ERR	$\mathrm{km\,s^{-1}}$	Uncertainty in v_{10}
6	OIII_V25	$\mathrm{km\,s^{-1}}$	[O III] v_{25}
7	OIII_V25_ERR	$\mathrm{km\,s^{-1}}$	Uncertainty in v_{25}
8	OIII_V50	$\mathrm{km\,s^{-1}}$	[O III] v_{50}
9	OIII_V50_ERR	$\mathrm{km\,s^{-1}}$	Uncertainty in v_{50}
10	OIII_V75	$\mathrm{km\,s^{-1}}$	[O III] v_{75}
11	OIII_V75_ERR	$\mathrm{km\,s^{-1}}$	Uncertainty in v_{75}
12	OIII_V90	$\mathrm{km\,s^{-1}}$	[O III] v_{90}
13	OIII_V90_ERR	$\mathrm{km\,s^{-1}}$	Uncertainty in v_{90}
14	OIII_V95	$\mathrm{km\,s^{-1}}$	[O III] v_{95}
15	OIII_V95_ERR	$\mathrm{km\,s^{-1}}$	Uncertainty in v_{95}
16	z_OIII		[O III] redshift
17	z_OIII_ERR		Uncertainty in [O III] redshift
18	OIII_W50	$\mathrm{km\,s^{-1}}$	[O III] w_{50}
19	OIII_W50_ERR	$\mathrm{km\,s^{-1}}$	Uncertainty in [O III] w_{50}
20	OIII_W80	$\mathrm{km\,s^{-1}}$	[O III] w_{80}
21	OIII_W80_ERR	$\mathrm{km\,s^{-1}}$	Uncertainty in [O III] w_{50}
22	OIII_W90	$\mathrm{km\,s^{-1}}$	[O III] w_{90}
23	OIII_W90_ERR	$\mathrm{km\,s^{-1}}$	Uncertainty in [O III] w_{50}
24	OIII_A		[O III] asymmetry
25	OIII_A_ERR		Uncertainty in [O III] asymmetry
26	OIII_EQW	Å	[O III] EQW
27	OIII_EQW_ERR	Å	Uncertainty in [O III] EQW
28	OIII_LUM	$\mathrm{erg\,s^{-1}}$	[O III] luminosity
29	OIII_LUM_ERR	$\mathrm{erg\,s^{-1}}$	Uncertainty in [O III] luminosity
30	EQW_FE_4434_4684	Å	Fe II EQW
31	EQW_FE_4434_4684_ERR	Å	Uncertainty in Fe II EQW
32	HB_VPEAK	$\mathrm{km\,s^{-1}}$	Hβ peak velocity
33	HB_VPEAK_ERR	$\mathrm{km\,s^{-1}}$	Uncertainty in Hβ peak velocity
34	HA_VPEAK	$\mathrm{km\,s^{-1}}$	Hα peak velocity
35	HA_VPEAK_ERR	$\mathrm{km\,s^{-1}}$	Uncertainty in Hα peak velocity
36	HB_Z		Hβ redshift
37	HB_Z_ERR		Uncertainty in Hβ redshift
38	HA_Z		Hα redshift
39	HA_Z_ERR		Uncertainty in Hα redshift
40	OIII_REDCHI		Reduced-χ^2 in Hβ/[O III] fit
41	OIII_FE_FLAG		Bad Fe II subtraction
42	OIII_EXTREM_FLAG		Extreme [O III] emission
43	HA_REDCHI		Reduced-χ^2 in Hα fit

We therefore choose to characterize the [O III] line profile using a number of non-parametric measures, which are commonly used in the literature (e.g. Zakamska and Greene, 2014; Zakamska et al., 2016). A normalised cumulative velocity distribution is constructed from the best-fitting model, from which the velocities below which 5, 10, 25, 50, 75, 90, and 95 per cent of the total flux accumulates can be calculated. These velocities are then adjusted so that the peak of the [O III] emission is at 0 $\mathrm{km\,s^{-1}}$.

The width of the emission-line can then be defined using either w_{50} ($\equiv v_{75} - v_{25}$), w_{80} ($\equiv v_{90} - v_{10}$) or w_{90} ($\equiv v_{95} - v_5$). In terms of the FWHM, $w_{50} \simeq \mathrm{FWHM}/1.746$, $w_{80} \simeq \mathrm{FWHM}/0.919$, $w_{90} \simeq \mathrm{FWHM}/0.716$, assuming a Gaussian line profile. w_{90} is relatively more sensitive to the wings of the line profile, whereas w_{50} is relatively more sensitive to the core. We also define the relative asymmetry of the line as:

$$A = \frac{(v_{90} - v_{\mathrm{peak}}) - (v_{\mathrm{peak}} - v_{10})}{(v_{90} - v_{10})}. \tag{1.1}$$

Line-width measures are corrected for instrumental broadening by subtracting the resolution of the spectrograph (Table **??**) in quadrature. Because the line profiles are typically non-Gaussian, this deconvolution procedure is only approximate. All of the derived parameters we have calculated are summarised in Table 1.5. The columns are as follows:

Paul: what about the 200 $\mathrm{km\,s^{-1}}$ (can't read)

1 Unique ID: QSOXXX.

2-3 Systemic redshift measured at [O III] peak wavelength, and its error.

4-17 v_5, v_{10}, v_{25}, v_{50}, v_{75}, v_{90} and v_{95} velocity of [O III], relative to [O III] peak, and their errors, in $\mathrm{km\,s^{-1}}$.

18-23 w_{50} ($\equiv v_{75} - v_{25}$), w_{80} ($\equiv v_{90} - v_{10}$) and w_{90} ($\equiv v_{95} - v_5$) velocity width of [O III], and their errors, in $\mathrm{km\,s^{-1}}$.

24-25 Dimensionless [O III] asymmetry A, and its error.

26-27 Rest-frame [O III] EQW, and its error, in Å.

28-29 1-σ upper-limit on rest-frame [O III] EQW, in Å.

30-31 [O III] luminosity, and its error, in $\mathrm{erg\,s^{-1}}$.

32-33 4434-4684 Ârest-frame Fe II EQW, and its error, in Å.

34-35 Velocity of Hβ peak, relative to [O III] peak, in km s^{-1}, and its error.

36-37 Velocity of Hα peak, relative to [O III] peak, in km s^{-1}, and its error.

38-38 Redshift of Hβ peak, and its error.

40-41 Redshift of Hα peak, and its error.

42 Reduced χ-squared from [O III]/Hβ fit.

43 Reduced χ-squared in fit to Hα .

44 Fe II flag.

45 Extreme [O III] flag.

46-47 C IV v_{50}, relative to [O III] peak, in km s^{-1}, and its error.

1.3.7 *Deriving uncertainties on parameters*

Our method to estimate realistic uncertainties on emission-line properties derived from the best-fitting model is very similar to the one describe in Chapter **??**. Very briefly, random simulations of each spectrum are generated. Our fitting-procedure is run on each simulated spectrum, and the errors on the line parameters are estimated by looking at the distribution of values from the ensemble of simulations. In a slight modification of the procedure in Chapter **??**, the error is defined using the 68 (84 - 16) percentile spread in the parameter values.

1.3.8 *The significance of [O III] detections*

We require a method of determining whether a measured EQW is significant or not. We measure the rms of the flux density in the emission-line free window between 4500 and 4600 Å. We multiply the rms by the wavelength per pixel, and then multiply this by the square root of the number of pixels in the full width at zero intensity of the [O III] profile, to get σ. A line flux is accepted as significant if it is $> 3\sigma$. We also adopt an EQW of 1Å as the lower detection limit to account for systematic errors.

σ not the same as upper limit derived above.

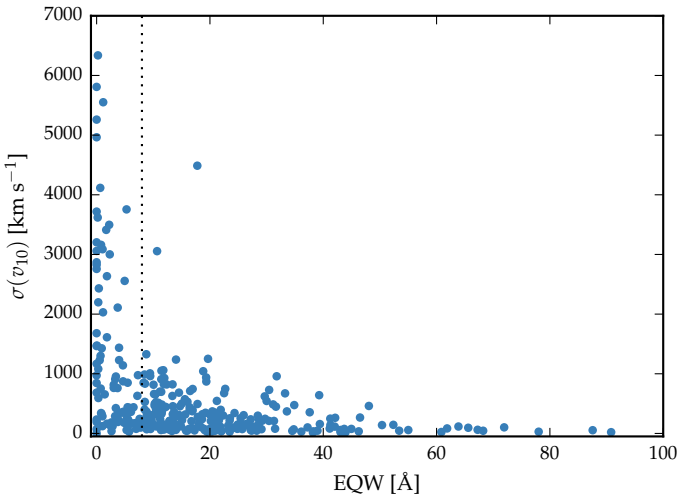

Figure 1.3: Uncertainty in v_{10} as a function of the EQW, for [O III]. Uncertainties in v_{10} are large to the left of the vertical line, at 8Å. These objects are ignored in our subsequent analysis of the [O III] line shape.

1.3.9 *Low EQW [O III]*

In Figure 1.3 we show how the uncertainty in v_{10} depends on the EQW. As the strength of [O III] decreases, the average uncertainty in v_{10} increases. As the EQW drops below 8Å, typical uncertainties in v_{10} become very large (exceeding 1000 km s^{-1}in many objects). Clearly, the emission-line is too weak for properties - in this case v_{10} - to be reliably measured in many of these objects. Therefore, when the [O III] line properties (e.g. velocity-width, centroid) are analysed in later sections, these objects with EQW $<$ 8Å will be excluded. This leaves 226 quasars in the sample.

1.3.10 *Reliability of redshift estimates*

In this section, we compare systemic redshift estimates based on [O III], Hβ and Hα. The wavelength of each of these lines is measured at the peak of the emission and this measurement is made using the best-fitting parameter model. In the case of the Balmer lines, this model includes both broad and (if present) narrow emission features.

We compare systemic redshift estimates based on [O III] and Hβ (Figure 1.4a), [O III] and Hα (Figure 1.4b) and Hβ and Hα (Figure 1.4c). [O III], Hβ and Hα measurements are avail-

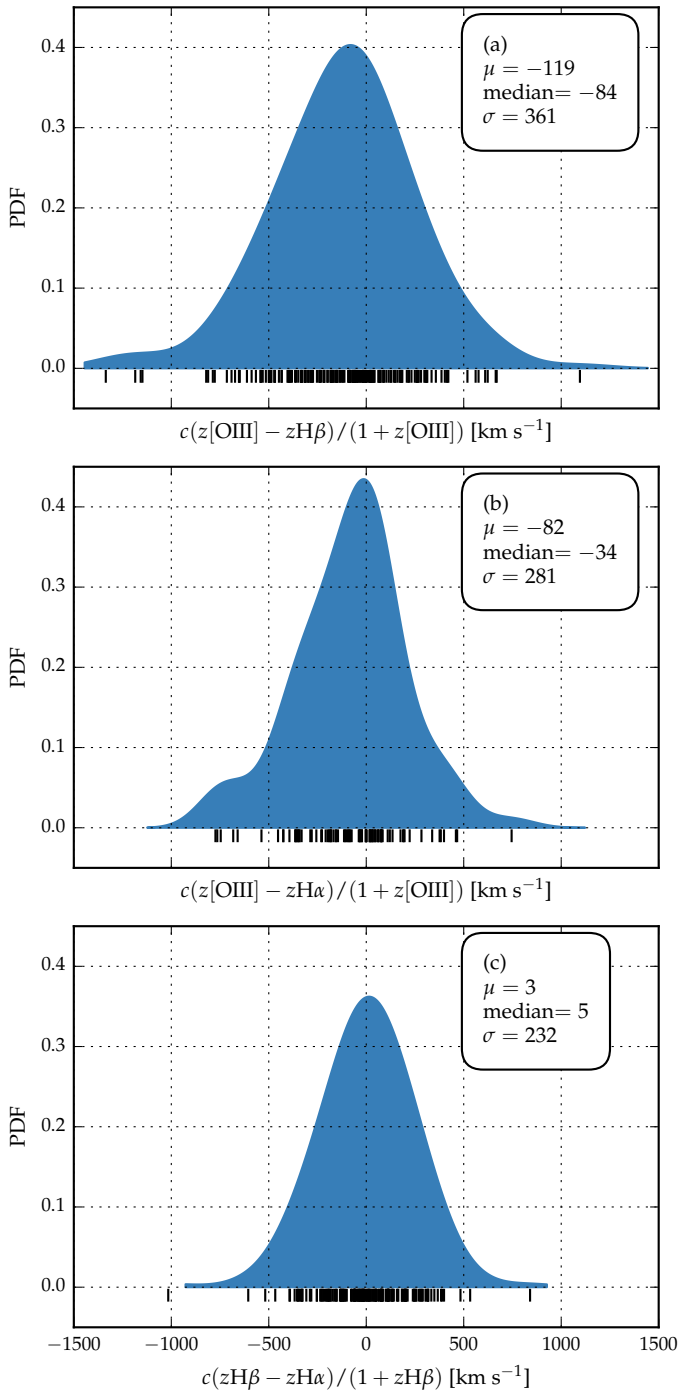

Figure 1.4: Comparison of systemic redshift estimates using [O III], broad Hβ and broad Hα. The probability density functions are generated using a Gaussian kernel density estimator with a $\simeq 150$ km s^{-1}kernel width. The short black lines show the locations of the individual points.

able for 226, 418 and 226 objects. We exclude [O III], Hβ and Hα measurements when the uncertainties on the peak velocities exceed 400, 600 and 400 km s^{-1}respectively. This excludes 4, 6 and 12 per cent of the [O III], Hβ and Hα measurements respectively. We also exclude [O III] measurements from 16 objects with very broad, blueshifted [O III] emission that is strongly blended with the red wing of Hβ (these objects are discussed in Section 1.6) because these redshifts are almost certainly strongly biased. After these cuts, there are 182, 85 and 162 objects being compared in samples (a), (b) and (c) respectively.

We generate probability density functions using a Gaussian kernel density estimator. The bandwidth, which is optimised using leave-one-out cross-validation, is 170, 120 and 140 km s^{-1}for samples (a), (b) and (c) respectively. The systematic offset between the Hα and Hβ estimates is consistent with being zero, and the scatter is 230 km s^{-1}. The scatter in these distributions is consistent with previous studies of redshift uncertainties from broad emission-lines (e.g. Shen et al., 2016). The [O III] redshifts appear to be systematically offset in comparison to both Hα and Hβ , in the sense that [O III] is blueshifted. This effect is strongest when [O III] is compared to Hβ , in which case [O III] is shifted by $\sim$ 100 km s^{-1}to the blue.

Paul: in the same sense as Heckman 1981 and HW10

1.4 RESULTS

Highlight key results more prominantly

In our sample of 354 quasars, there is a huge diversity in [O III] emission properties (Fig. 1.2). In Figure **??** we present a sub-set of the measurements we have made of the [O III] line.

The [O III] EQW follows an approximately log-normal distribution, peaking at 17Å. In 10 per cent of our sample [O III] is very weak, with EQW $<$ 1 Å. The average [O III] strength is consistent with earlier studies on smaller samples (e.g. Sulentic et al., 2004; Netzer et al., 2004; Shen, 2016). The strength of [O III] depends on the covering factor of NLR gas, its density and ionisation parameter.

Paul: Define undetected as less than 3σ?

The mean and standard deviation of the line width (characterized by w_{80}) is 1535$\pm$562 km s^{-1}, with a median of 1529, minimum of 206 and maximum of 3214. This is consistent with recent near-infrared spectroscopy of $z > 1.5$ quasars which often report velocity widths $\gtrsim$ 1000 km s^{-1}(e.g. Netzer et al., 2004; Kim et al., 2013; Brusa et al., 2015; Shen, 2016).

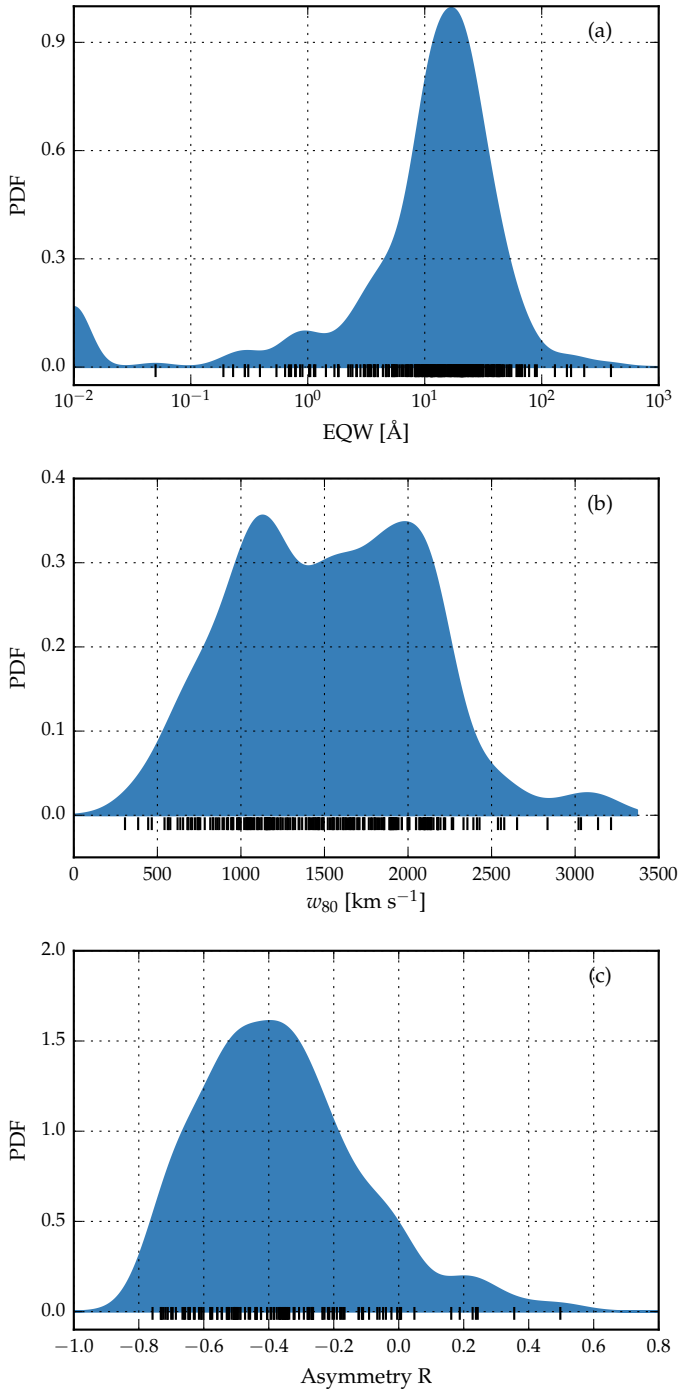

Figure 1.5: Probability density distributions of the [O III] parameters EQW (a), w_{80} (b) and asymmetry R (c).

For gas discs rotating in the potential of the massive galaxies line widths do not exceed $w_{80} \simeq 600$ km s^{-1}(Liu et al., 2013). Therefore the [O III] gas cannot be in dynamical equilibrium with the host galaxy. [O III] emission is suppressed by collisional de-excitation in higher-density environments, and so the large velocity widths cannot be due to the BLR. The 1200 km s^{-1}upper limit on the velocity width of the Gaussian functions used to model [O III] is responsible for the peak at 1200 km s^{-1}.

The [O III] asymmetry is shown in Figure 1.5c. In 40 per cent of the sample [O III] is fit with a single Gaussian. The asymmetry is zero in this model and so these objects are excluded. [O III] is blue-asymmetric in all but a handful of objects. This indicates that there is an outflow component in the [O III]-emitting gas. We also find that there is a correlation between w_{80} and the asymmetry: the broader lines are more blue-asymmetric.

1.4.1 *Luminosity/redshift-evolution of [O III] properties*

Comparison sample

We extend the dynamic range of our samples in terms of both luminosity and redshift by supplementing our sample with quasars presented by Mullaney et al., (2013) and Harrison et al., (2016). The Mullaney et al., (2013) catalogue contains [O III] line measurements for ~25 000 optically-selected AGN with SDSS spectra at $z < 0.4$. Mullaney et al., (2013) fit [O III] with one or two Gaussians, and then used similar non-parametric measures to the ones we adopt. We select only the Type I AGN from the Mullaney et al., (2013) catalogue. The Harrison et al., (2016) sample contains 40 quasars at intermediate redshifts ($1.1 \leqslant z \leqslant 1.7$).

We also use the SDSS DR7 quasar catalogue, with properties derived by Shen et al., (2011). [O III] is visible in SDSS spectra up to redshifts $z = 0.84$. There are 20,663 quasars in the Shen et al., (2011) catalogue with [O III] EQW > 0Å.

Equivalent width

In Fig. 1.6 we show the [O III] EQW as a function of the quasar bolometric luminosity. Bolometric luminosity is estimated from the monochromatic continuum luminosity at 5100Å, using the

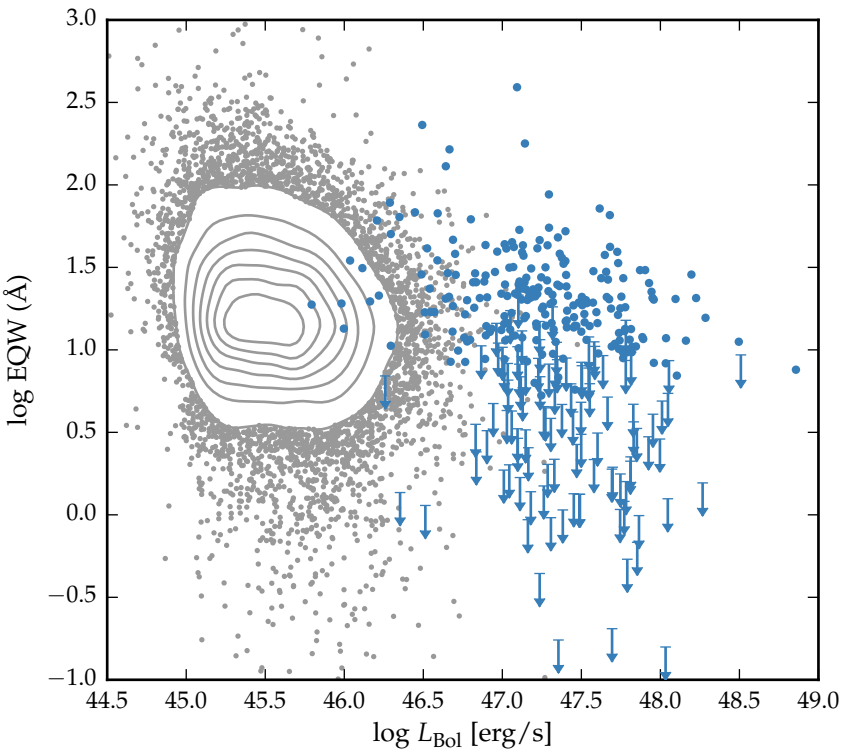

Figure 1.6: The [O III] EQW as a function of the quasar bolometric luminosity for the sample presented in this chapter (blue circles) and the low-z SDSS sample (grey points and contours). Upper limits are denoted by the downward arrows. Use upper limit when EQW less than 3σ?

correction factor given by Richards et al., (2006). For comparison, we also show the low-z sample from Shen et al., (2011).

We find that [O III] EQW is fairly constant as a function of quasar luminosity in the objects with prominent [O III] emission. We find that [O III] is undetected/very weak in XX per cent of our sample, which is very similar to the fraction reported by Netzer et al., (2004) based on a much smaller sample. In contrast, quasars with weak [O III] are very rare in nearby AGN. As a result, the mean [O III] EQW decreases as a function of luminosity (e.g. Brotherton, 1996; Netzer et al., 2004; Sulentic et al., 2004; Baskin and Laor, 2005). This trend is known as the Baldwin effect for [O III] (e.g. Baldwin, 1977; Brotherton, 1996; Zhang et al., 2011; Stern and Laor, 2012).

Explain why Baldwin effect - gas photoinoised by accretion disc. as you have more ionising photons the NLR grows, but then there is no more gas to inoise and the size plateus. What

is Netzer interpretation? Plot the EQW strength as a function of luminosity (Show histograms?)

Theoretical suggestions that the NLR size should scale with the square root of L_Hb (e.g. Netzer 1990). Similar to the R-L relation scaling fro the BLR. This seems to be confirmed in low luminosity AGN. Howver, it raises severe problems for high luminosity quasars. Any such scaling leads to sizes that are larger than galactic sizes. Typical NLRs (those similar in properties to ones in Seyferts) cannot last very long in high luminosity quasars, because they have galactic dimensions and are likely to excape the system. This means that when we have strong [O III] it may be of a different origin and physical properties. In particular the gas densities must be orders of magnitude larger. A possible origin of this high density gas in kpc scale nuclear regions is violent star formation.

1.4.2 *Velocity width*

In Figure 1.7 we show the [O III] velocity width as a function of the [O III] luminosity and the quasar redshift. The lack of any redshift-evolution between $z = 0$ and $z = 1.5$ was reported by Harrison et al., (2016). The kinematics of high redshift quasars are similar to those at lower redshifts with similar luminosities. On the other hand, at fixed redshift, we see a significant correlation between the [O III] velocity width and the luminosity.

1.5 EIGENVECTOR 1 CORRELATIONS

1.5.1 *EV1 trends exist in high-redshift quasars*

The FWHM of the broad Hβ emission-line and the relative strengths of optical Fe II and Hβ have been identified as the features responsible for the largest variance in the spectra of AGN. These parameters form part of EV1, the first eigenvector in a PCA which originated from the work of Boroson and Green, (1992). The underlying driver behind EV1 is thought to be the Eddington ratio (e.g. Sulentic et al., 2000; Shen and Ho, 2014).

In Figure 1.8 we show the [O III] EQW as a function of the Hβ FWHM and the optical Fe II strength. The optical Fe II strength is defined as the ratio of the Fe II and Hβ EQW, where the Fe II EQW is measured between 4434 and 4684Å. Measurements of the Hβ line properties are taken from Chapter **??**.

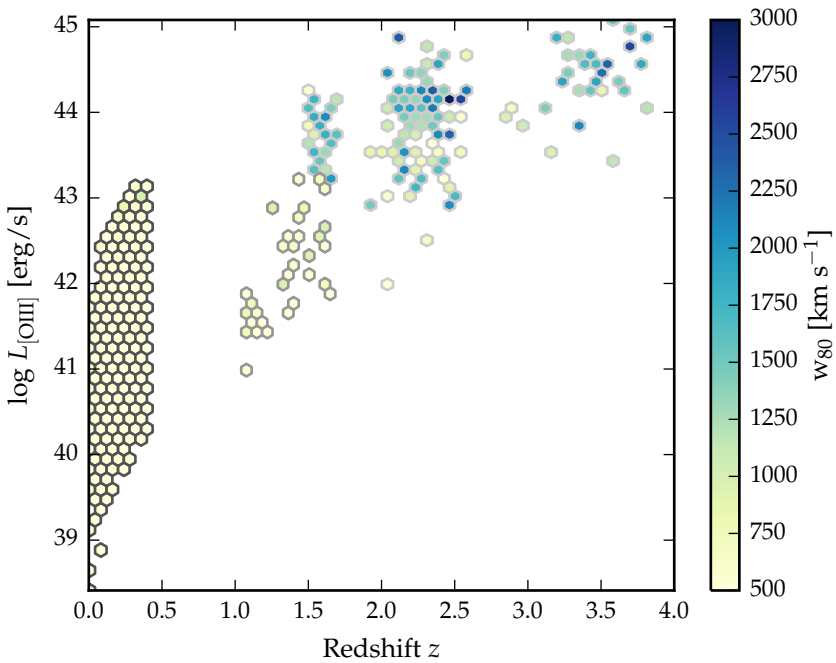

Figure 1.7: The [O III] velocity-width, characterised by w_{80}, as a function the [O III] luminosity and the quasar redshift. The colour of each hexagon denotes the mean w_{80} for the objects in that luminosity-redshift bin. Objects at redshifts $z < 0.5$ are from Mullaney et al., (2013), lower-luminosity objects at redshifts $z \sim 1.5$ (with a darker grey border) are from Harrison et al., (2016), and objects with a light grey border at $z \gtrsim 1.5$ are from this Chapter.

In our sample, these parameters follow very similar correlations to what is observed at low-z. In particular, we observer a strong anti-correlation between the [O III] and Fe II EQW. The Hβ FWHM are displaced to higher values, which is consistent with the high-redshift, high-luminosity sample having larger BH masses. Thus, we confirm earlier results using much smaller samples that suggest that the same EV1 correlations exist in high-redshift quasars (e.g. Netzer et al., 2004; Sulentic et al., 2004; Sulentic et al., 2006; Runnoe et al., 2013; Shen, 2016).

histogram RFeii? do we see typically stronger iron suggesting higher accretion rates?

1.5.2 *Extending EV1 parameter space*

The C IV blueshift and EQW is a diagnostic that similarly spans the diversity of broad emission-line properties in high redshift quasars (Sulentic et al., 2007; Richards et al., 2011). C IV is dominated by a virialized component at one extreme, and is domi-

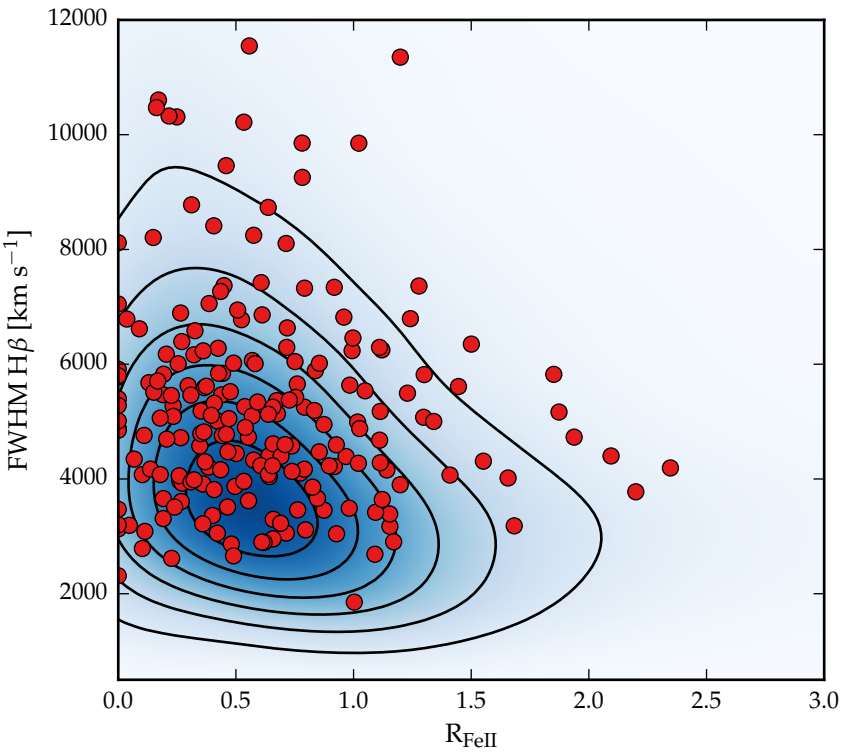

Figure 1.8: EV1 parameter space. The contours and shading show low-redshift, low-luminosity SDSS AGN (with measurements taken from Shen et al., (2011)) and the red circles show the high-redshift, high-luminosity objects presented in this chapter.

nated by outflows at the other (see Chapter **??** for details). The similarity of the C IV EQW-blueshift parameter space at high redshift to EV1 parameter space at low redshift suggests that these trends are connected.

Optical spectra are available for XXX quasars in our catalogue, and cover the broad C IV doublet. In Chapter **??**, we demonstrated that the quasars in our sample cover the full range of C IV blueshifts seen in the SDSS quasar population. This means that we can use our quasar sample to understand how the low-redshift EV1 parameter space maps to the high-redshift C IV parameter space. In Figure 1.9 we show how the EV1 parameters change as a function of position in the C IV EQW-blueshift parameter space.

Two hundred and fourteen objects are shown in Figure 1.9. Objects for which the Hβ or C IV line properties could not be measured reliably (see Section **??**) have also been removed. We consider only objects for which the C IV EQW exceeds 15Å. The

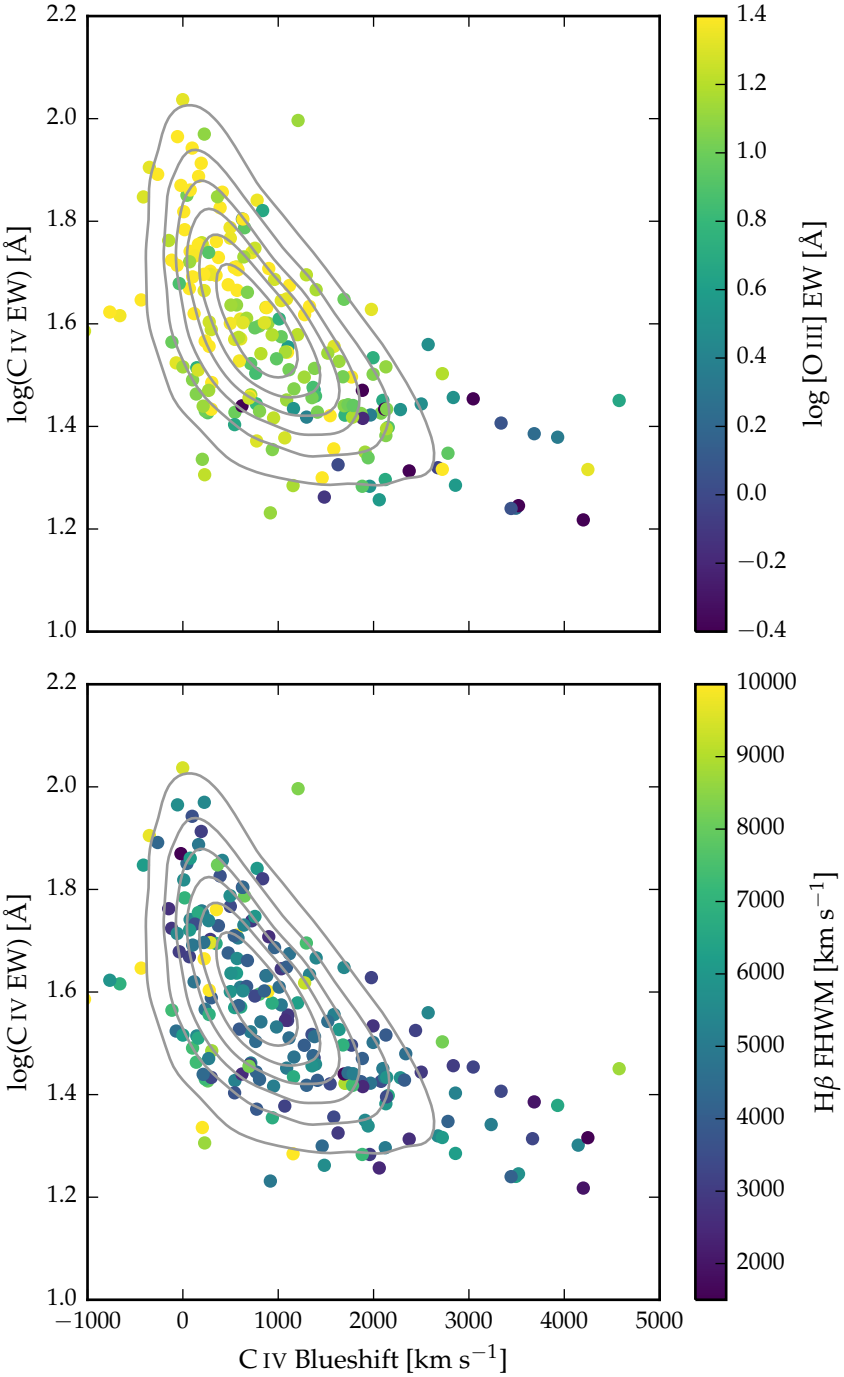

Figure 1.9: The high-redshift EV1 parameter space of C IV blueshift and EQW. Our sample is shown with points, and quasars from the full SDSS catalogue are shown with grey contours. The [O III] EQW varies systematically with position in the C IV blueshift-EQW parameter space (a) but the Hβ FWHM shows significantly less systematic variation (b).

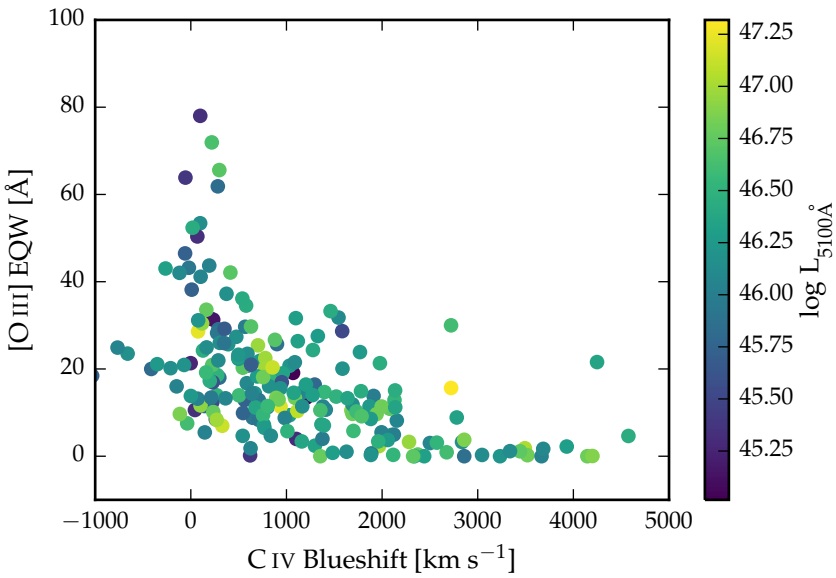

Figure 1.10: [O III] EQW as a function of the C IV blueshift.

C IV blueshift is measured relative to the redshift determined from the peak of [O III], Hβ or Hα.

Most of the diversity in C IV properties is correlated with the [O III] EQW. This is seen more clearly in Fig. 1.10, in which we plot the [O III] EQW as a function of the C IV blueshift. On the other hand, the C IV blueshift and EQW cannot be used to predict the Hβ FWHM. This is consistent with what we found in Chapter **??**: objects with large C IV blueshifts have narrow Balmer emission-lines, but objects with modest C IV blueshifts have a wide range of Balmer line widths.

1.6 EXTREME [O III] EMITTERS

Figure **??** shows the spectra of 18 objects which we visually identified as having exceptionally broad [O III] emission profiles. These objects are defined as having very broad [O III] emission (although not necessarily the broadest in our sample) and heavily blended emission in between the zero-velocity wavelengths of Hβ and [O III]. Because the emission is so heavily-blended, it is difficult to determine unambiguously what combination of Hβ , [O III] and Fe II is responsible for the unusual plateau-like emission observed in these objects. Therefore, uncertainties on the [O III] emission properties are generally high in these objects.

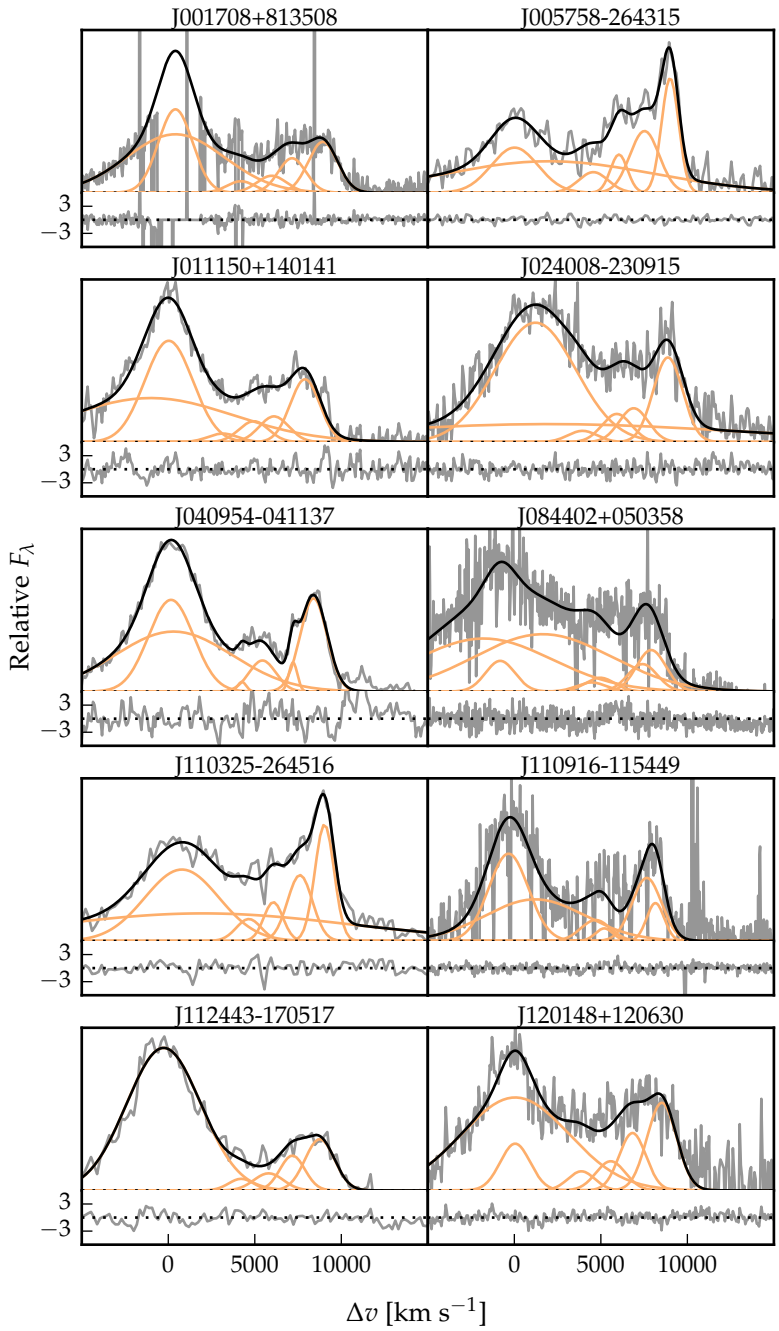

Figure 1.11: Model fits to the continuum- and Fe II-subtracted Hβ/[O III] emission in 18 quasars with extreme [O III] emission profiles. The data is shown in grey, the best-fitting model in black, and the individual model components in orange. The peak of the [O III] emission is used to set the redshift, and Δv is the velocity shift from the rest-frame transition wavelength of Hβ . Below each spectrum we plot the data minus model residuals, scaled by the errors on the fluxes.

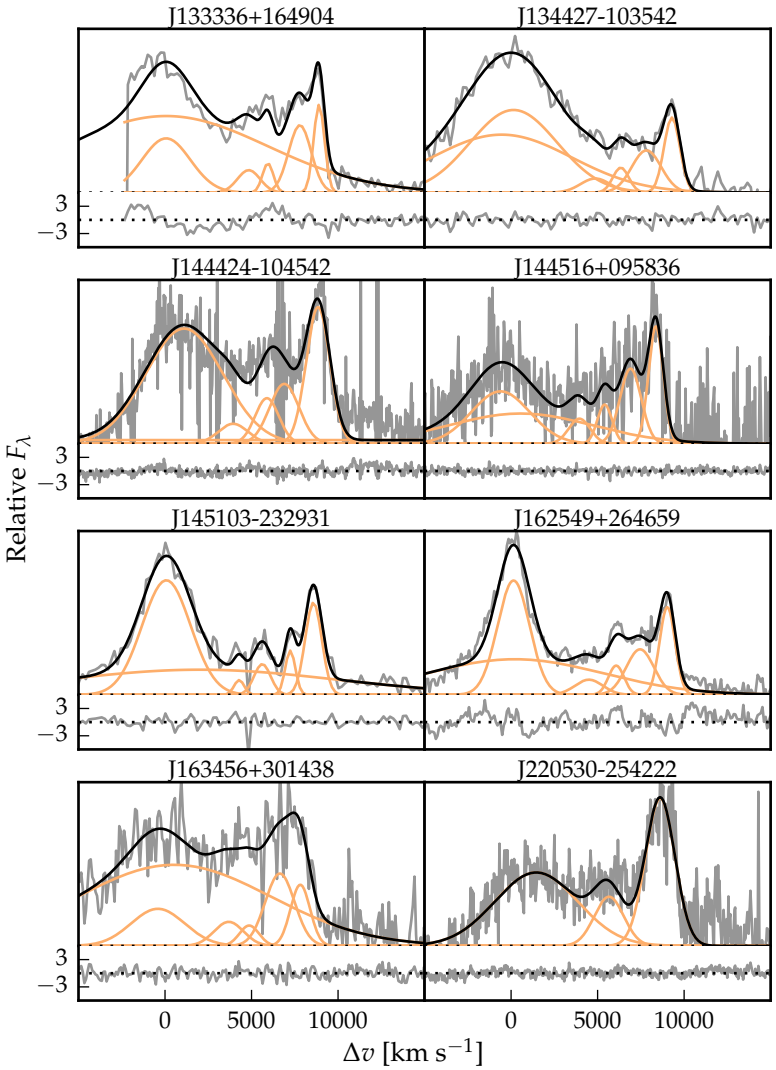

Figure 1.11: Continued.

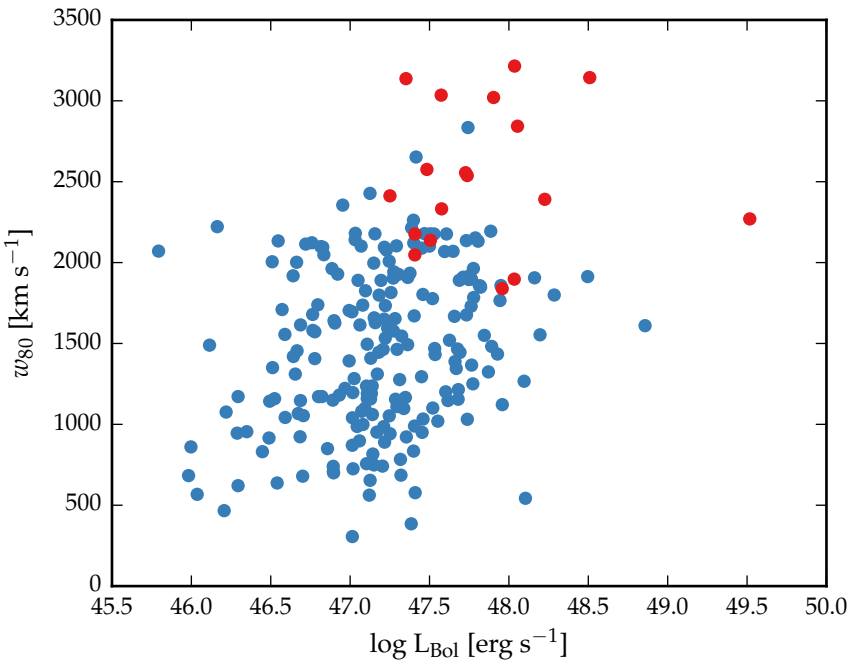

Figure 1.12: [O III] velocity width as a function of quasar bolometric luminosity. Objects with extreme [O III] profiles are shown in red.

In Figure 1.12 we show that the luminosities of all of these objects are larger than the sample median.

These [O III] emission-lines are similar to the lines observed in a sample of four extremely dust-reddened quasars at $z \sim 2$ recently identified by Zakamska et al., (2016). The extreme nature of the [O III] emission in these objects led Zakamska et al., (2016) to propose that these objects are being observed transitioning from a dust-obscured, star-burst phase to a luminous, blue quasar. A similar [O III] emission was also observed in J1201+1206 in a sample of five of the most luminous quasars at redshifts $2.3 \lesssim z \lesssim 3.5$ observed by Bischetti et al., (2016).

The four Zakamska et al., (2016) quasars have 5 μm luminosities of $\sim 10^{47}$ erg s^{-1}, which is comparable to maximum luminosity of our sample. The [O III] velocity widths of the Zakamska et al., (2016) objects are extreme in relation to our sample, matched in 5 μm luminosity. The quasars in our sample have very modest amounts of dust reddening ($E(B-V) \sim 0.03$ on average). These findings therefore appear to support the idea that strong feedback is occurring in this population of heavily reddened quasars.

A couple of paragraphs above I same they are 'similar' so need to be consistent

1.6.1 *[O III] and C IV outflows are linked*

In Chapter **??** we looked in detail at properties of the C IV emission in luminous, high-redshift quasars. In many objects C IV is broad and blueshifted, which we interpret as evidence of strong outflows in the quasar BLR. These outflows can reach many thousands of $\mathrm{km\,s^{-1}}$. However, to quench star formation quasar-driven outflows must break out to galactic scales.

Earlier, we saw that the [O III] EQW has a very strong dependence on the C IV blueshift. [O III] is undetected in XX per cent of quasars with C IV blueshifts greater than 2000 $\mathrm{km\,s^{-1}}$.

In Figure 1.13 we show the the [O III] blueshift as a function of the C IV blueshift. The [O III] blueshift is defined as $v_{10} - v_{\mathrm{peak}}$. For the C IV blueshift we use v_{50} as a measure of the line location, and again use the peak of the [O III] emission to define the systemic redshift. We use the C IV velocity centroid measurements we derived in Chapter **??**. We take a subset of quasars with [O III] EQW $>$ 8Å. This removes most of the quasars with large C IV blueshifts, since [O III] is on average very weak in these quasars. We also remove objects where the fractional uncertainty on v_{10} exceeds 50 per cent (XX quasars).

There is a clear and strong correlation. [O III] is more blueshifted in quasars with large C IV blueshifts. This suggests a direct connection between the gas kinematics in the broad and narrow line regions.

We considered a number of of alternative approaches to parametrising both the [O III] line shape and the systemic redshift. As expected, very similar trends are observed when the [O III] line shape is parametrised using $v_{25} - v_{\mathrm{peak}}$, $v_{50} - v_{\mathrm{peak}}$, $w_{80} = v_{90} - v_{10}$, or the relative asymmetry R. The same trend is also observed when the systemic redshift is defined using the peak of the Hβ emission.

The blueshifting of C IV is known to correlate with luminosity (Richards et al., 2011). In [O III], the blueshifted wing becomes relatively more prominent as the luminosity of the quasar increases (Shen and Ho, 2014). Therefore, it is plausible that the correlation between the C IV and [O III] blueshifts is a secondary effect that is driven by the correlation of each with the luminosity. However, no strong luminosity-dependent trends are apparent in Figure 1.13. We find that both the [O III] and C IV blueshifts are correlated with the luminosity, but that these correlations are much weaker than the correlation between the [O III] and C IV blueshifts. *quantify weaker*

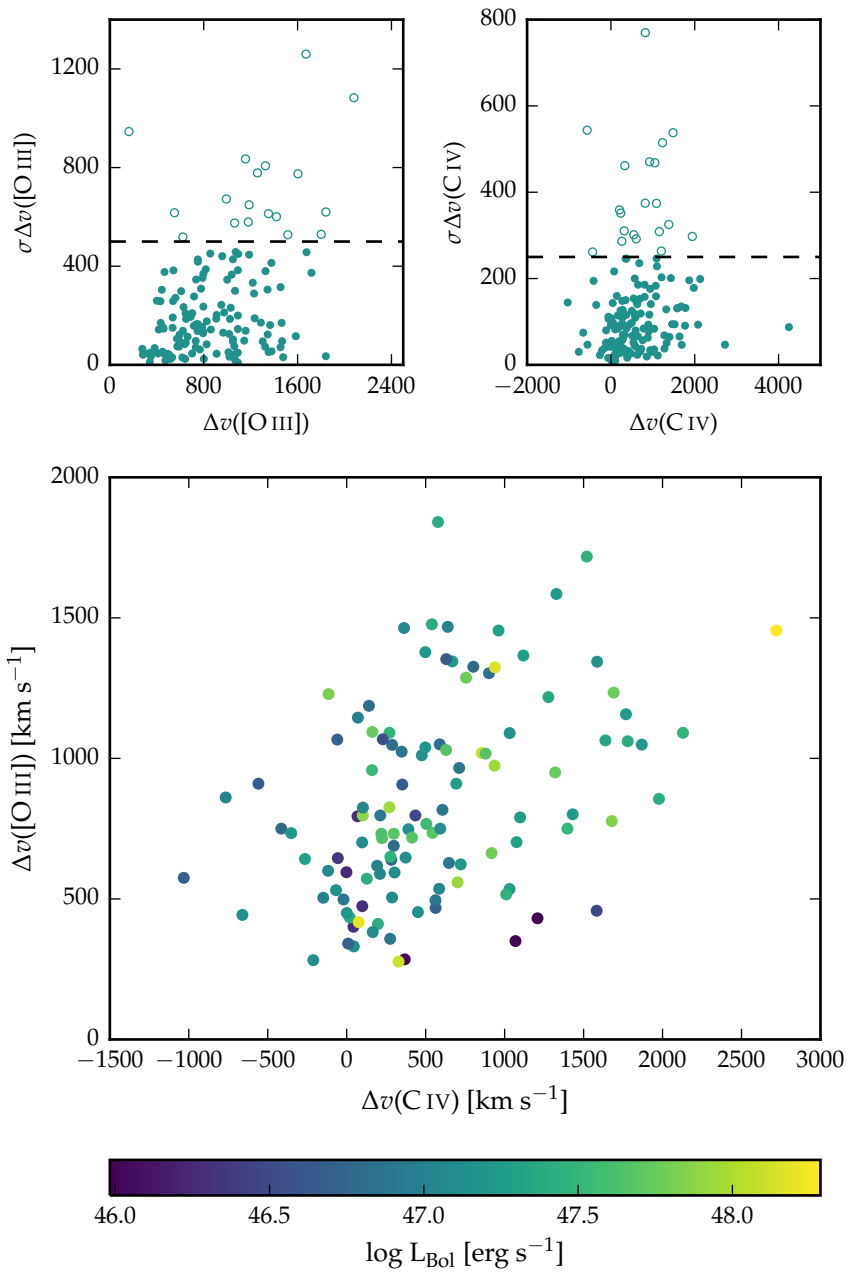

Figure 1.13: The relation between the blueshifts of C IV and [O III].

It has been known for some time that the [O III] EQW is anti-correlated with the strength of optical Fe II, and this trend is thought to be driven by the Eddington ratio. Shen and Ho, (2014) showed that the amplitude of the core [O III] emission decreases faster than the wing component as the Eddington ratio increases. Therefore, the [O III] emission is weaker and more blueshifted in high accretion rate quasars. In Chapter **??** we found that all quasars with strong BLR outflows have high Eddington ratios. In this section, we show that the C IV and [O III] blueshifts are directly linked. This suggests a direct connection between the gas kinematics in the broad and narrow line regions.

Discuss cuts

We don't show extreme objects

Similar correlations have been tentatively found in lower redshift quasars and AGN (Zamanov et al., 2002).

1.7 DISCUSSION

1.7.1 *Static NLR is removed by outflows*

Is the AGN NLR absent in objects where outflows have reached kilo-parsec scales, sweeping up the low-density material responsible for the [O III]-emission? If the BLR outflows can escape, they are very fast and wouldn't need long to clear out the NLR gas. Estimate a time-scale for how long the NLR would take to be cleared given typical size of galaxy and velocity of outflow.

READ ZAKAMSKA DISCUSSION

1.8 INDEPENDENT COMPONENT ANALYSIS

ICA better with S/N - can give some examples from PCA work (ask Paul for references). If the [O III] emission is confined to a relatively small number of components can then recover emission. Can show problem with w_{80} as an example. Encouraging, but we do need a better training set (training set doesn't span the diversity of properties we see in the high-luminosity sample). The content of the ICA "test" is fine but I would suggest setting up the experiment somewhat differently and orienting the reader at the start. For example I would mention a) the likely lack of sensitivity to S/N [cf standard approach], b) equating components with physical properties of interest and thus potential effectiveness of component weights (e.g. what is to come in Fig. 1.16). Would also though put in the information about using the SDSS objects to generate the component set and how one probably expects the high-luminosity sample to

include spectral diversity not present in the SDSS-sample [and hence in the ICA components]. You can, as you have drafted, then say how the analysis could be improved - better training set, removing the component cross-talk (I can tell you how this can be achieved),...

In this section, we consider an alternative approach to the analysis presented in the bulk of this Chapter. We use an independent component analysis (ICA) to separate the spectrum into a linear combination of statistically independent sub-components. Each individual spectrum can then be reconstructed with a linear combination of these components. The goal of this section is to determine whether or not the relative weights of the different components can be used in place of more commonly used emission-line parameters to understand the physical processes occurring in these quasars.

Issues with the parametric model fitting approach adopted above include sensitivity to S/N. We also found the empirical template to be a poor match to the Fe II emission observed in a number of quasars.

1.8.1 *The technique*

ICA is a blind source separation technique for separating a signal into linearly mixed statistically independent subcomponents. Unlike the more widely-used principle component analysis technique, ICA produces non-negative components which allows for a physical interpretation of the components and weights. ICA has been successfully applied to model the spectra of emission-line galaxies (Allen et al., 2013). The quasar spectra can be thought of as a set of observations, $\mathbf{x}$, which are made up of statistically independent components, $\mathbf{c}$, that are combined by some mixing matrix, $\boldsymbol{W}$:

$$\mathbf{x} = \boldsymbol{W}\mathbf{c} \tag{1.2}$$

ICA reverses this process and describes how the observed data are generated. Both the independent components and the mixing matrix are unknown, but can be found by solving:

$$\mathbf{c} = \boldsymbol{W}^{-1}\mathbf{x}. \tag{1.3}$$

The components were solved for using a sample of 2,154 SDSS quasars at redshifts XX. At these redshifts the SDSS spec-

Ask Paul for details.

trograph covers the rest-frame region XX-XXÅ where Hβ and [O III] lie. The individual spectra were first adjusted to give the same overall shape as a model quasar template spectrum. Six positive independent components and four lower-amplitude 'correction' components that could be negative were found to be sufficient to reconstruct the spectrum, without over-fitting. Each quasar spectrum x_j can then be represented as a linear combination of the independent components:

$$x_j = \sum_{i=1}^{10} c_{ij} W_{ij} \tag{1.4}$$

Fitting procedure

Each of the individual ICA components has been adjusted to give the same overall shape as a quasar template spectrum. We approximate the overall shape of this template by fitting a single power-law to emission-line free windows at 4200-4230, 4435-4700 and 5100-5535 Å. We then flatten each of the ICA components by dividing by this power-law. An identical process is performed on each spectrum we fit, so that both the components and the spectrum to be fitted have essentially zero large-scale slope. For each quasar in our sample we perform a variance-weighted least-squares minimisation to determine the optimum value of the components weights. The first six component weights are constrained to be non-negative, and the fit is performed in logarithmic wavelength space, so that each pixel corresponds to a fixed velocity width. The relative shift of the ICA components is also allowed to vary in the optimisation procedure, to account for errors in the systemic redshifts used to transform the spectra into rest-frame wavelengths.

1.8.2 *Quality of fits*

In general, the ICA components are able to reconstruct the spectra of the objects in our sample. We also find that that in some cases, the ICA reconstructions are superior at modelling the Fe II emission than the Boroson and Green, (1992) template.

Need something more quantative Look at chi-squared distribution? Doesn't seem that reliable.

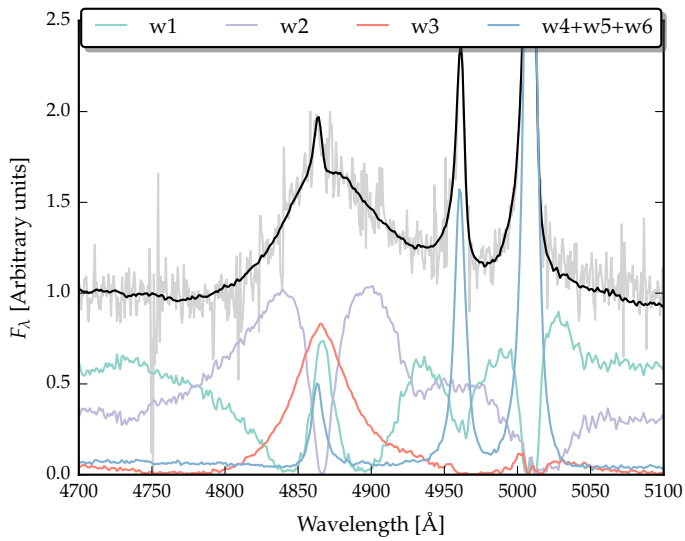

Figure 1.14: Hβ/[O III] emission J002952+020607. The ICA reconstruction is shown in black, and the spectrum in grey. The first three components, and the sum of components four, five and six are shown individually.

Table 1.6: Physical interpretation of the ICA components.

Component	Origin
w_1	Fe II
w_2	Hβ
w_3	Hβ
w_4	[O III] core
w_5	[O III] core
w_6	[O III] wing

1.8.3 *Physical interpretation of ICA components*

Although the ICA analysis is not based on any physics, there appears to be a direct correspondence between the individual non-negative components and the different emission features which contribute to the spectra (Fig. 1.14). This correspondence is summarised in Table 1.6. The component w_1 seems to correspond to Fe II emission, the components w_2 and w_3 to broad Hβ emission, the components w_4 and w_5 to narrow [O III] emission at the systemic redshift, and the component w_6 to broad, blueshifted [O III] emission. s

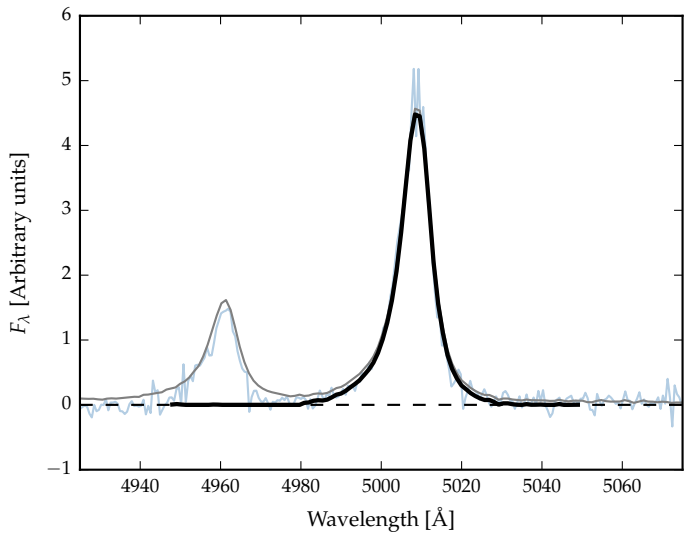

Figure 1.15: [O III] emission in J002952+020607. The data is shown in blue, and the ICA spectrum in grey. The first three ICA components have been subtracted from both the ICA composite and the data. The black curve shows the reconstructed [O III]λ5008 profile.

Reconstructing the [O III] profile

In order to measure non-parametric line parameters, e.g. v_{10}, we must first reconstruct the [O III] emission. It is fortunate that most of the [O III] emission is in just three of the ICA components; the remaining three contribute very little. Therefore, we can set the first three weights to zero to leave only the [O III] emission. The four correction components are also included.

We define the boundaries of [O III]λ5008 as being between 4950 and 5500Å. The blue limit is close to the peak of the [O III]λ4960 line, and so to recover the intrinsic profile we instead use the blue wing of [O III]λ4960. We use the emission from 4980-5050Å, and from 4900-(4980-(5008.2-4960.3)). The blue window is then shifted by (5008.2-4960.3) to reconstruct the blue wing of the [O III]λ5008 line. We then subtract a constant, because the flux does not always go to zero (suggests that there is probably flux which is not due to [O III] emission in components four to six).

An examples of a reconstructed [O III] emission-line is shown in Figure 1.15. At present I am summing the flux all the way from 4950Å. However, this is quite a lot of flux to sum up, and we can't ascribe this flux to the wing of the [O III] emission with any certainty. This is borne out by the fact that there are quite

Paul - include figure because description is complicated. But I might ditch this altogether.

large differences between, for example, v_{10} measured from the Gaussian fit and v_{10} measured from the ICA fit.

Paul: Think you need to say something about the SDSS quasar sample which was used to generate the ICA components. I woul at that point herald that the limited spectral diversity in the SDSS sample is likely to prove an issue, even if the ICA aproach looks promising.

Unfortunately, there are systematic differences between the line-width estimates from the Gaussian reconstructions and the ICA reconstructions, particularly for broad-line objects. The current way of doing the ICA reconstruction of the [O III] line ignores any cross-talk between the components and there is potentially flux being ascribed to the line that could be coming from some other component. We can solve this by finding some more representative broad [O III] lines in SDSS from which to derive the components as well as producing a set of components for [O III] only. Therefore we don't use these reconstructions and leave this for future work.

1.8.4 *ICA fits*

In Figure 1.16 we show the relative weights of each of the six positive ICA components. Also shown are the same measurements for a sample of low-redshift, low-luminosity AGN. We want to examine whether or not there are systematic differences between these two samples.

Paul: Paragraph belongs with material above

We see that [O III] core emission is weaker in the more luminous sample, but the strength of the wing component is similar. Shen and Ho, (2014) showed that the strength of the core [O III] component decreases with quasar luminosity and optical Fe II strength faster than the wing component, leading to overall broader and more blueshifted profiles as luminosity and Fe II strength (or C IV blueshift) increases. Shen and Ho, (2014) suggested that a stable NLR is being removed by the outflowing material. Similarly, Zhang et al., (2011) found that the more the peak of the [O III] line is blueshifted, the more the core component decreases dramatically, while the blue wing changes much less. Therefore, there is an anti-correlation between the strength of the core component and the relative strength of the wing component (Figure 1.18).

To show this phenomenon more clearly, we plot the relative [O III] strength and the [O III] wing/core ratio in the high/low luminosity samples (Figure 1.18). We see that [O III] is weaker in the high luminosity sample, but that the wing component is much stronger relative to the core component. .

Similar to behaviour of C IV? Would suggests that the mechanism producing the two correlations is the same

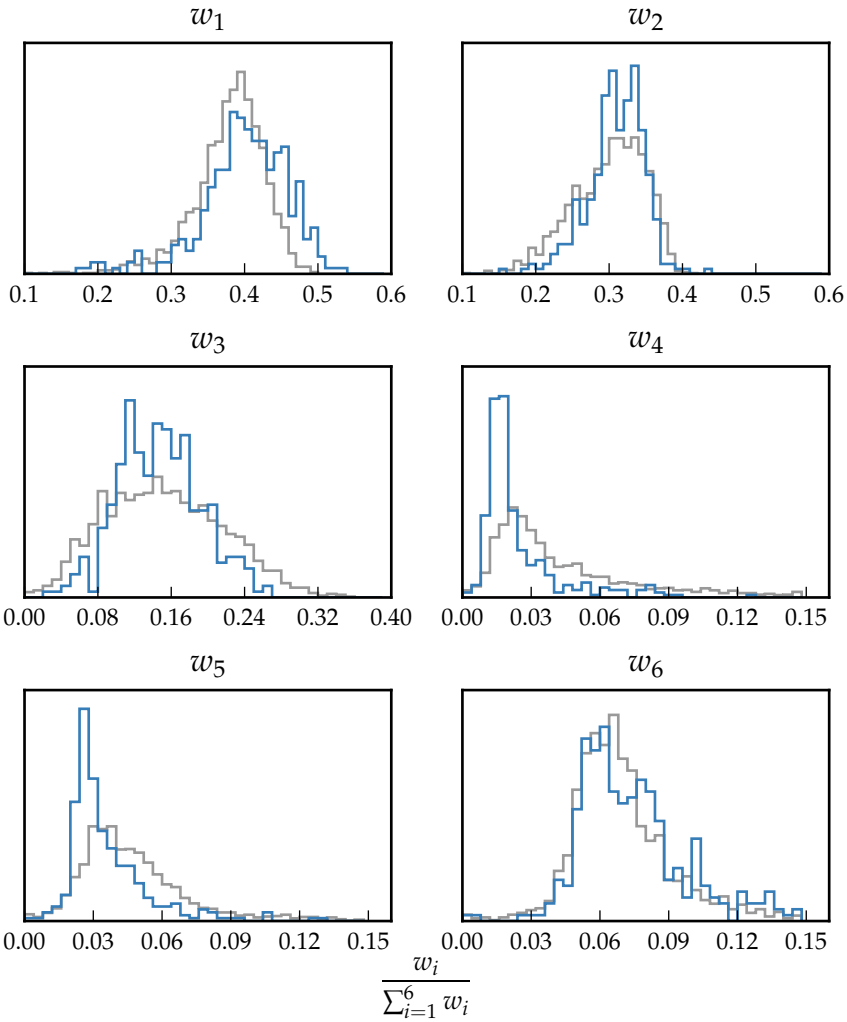

Figure 1.16: The relative weight in each of the six positive ICA components for the high-luminosity (blue) and low luminosity samples (grey). In the high-luminosity sample Fe II emission is stronger (component w_1). The core [O III] emission (components w_4, w_5) is weaker but the strength of the blueshifted wing (w_6) is the same.

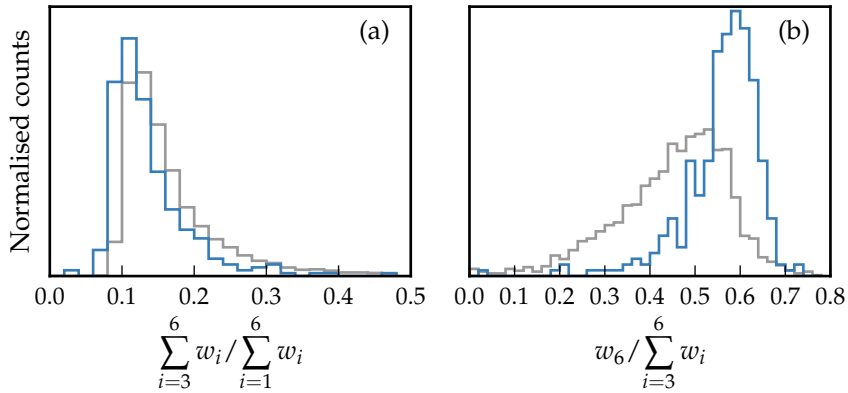

Figure 1.17: The relative weight in the three ICA components corresponding to [O III] emission (*left*) and the relative weight of the component most closely related to blueshifted [O III] emission relative to all three [O III] components (*right*). [O III] emission is weaker in the high-luminosity sample, but the relative contribution from the blueshifted component to the total [O III] emission is higher.

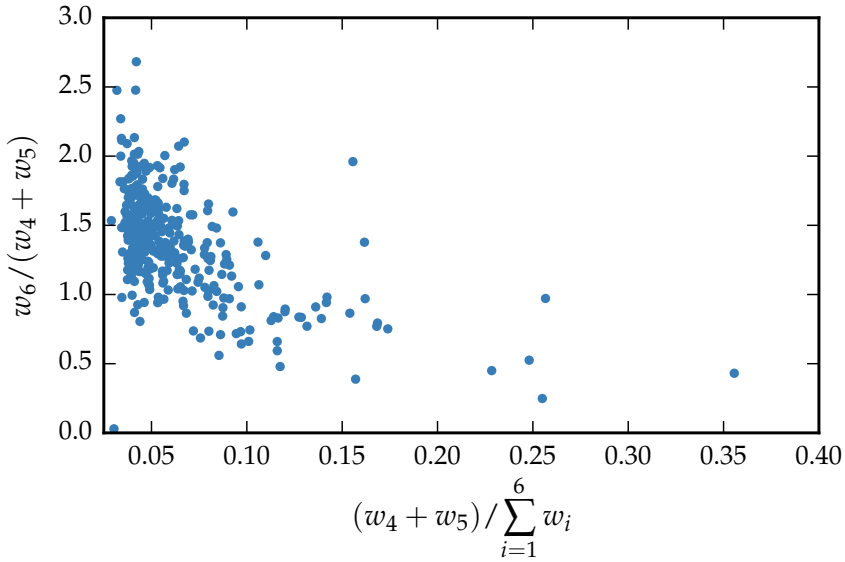

Figure 1.18: Weight in the [O III] wing relative to the weight in the [O III] core emission versus the strength of the core [O III] emission. The blue-asymmetry of the [O III] emission increases as the strength of the core component decreases.

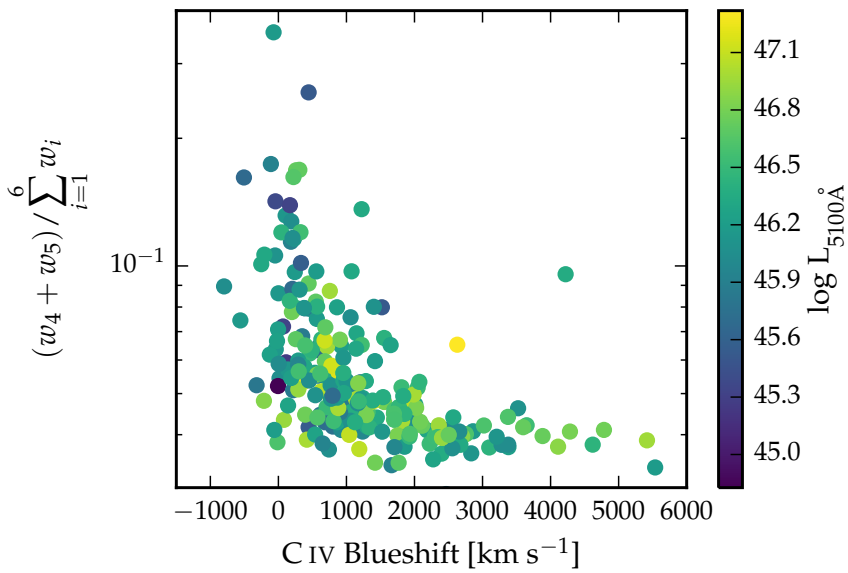

Figure 1.19: The ICA component weight w_4, which is a proxy for the strength of core [O III], as a function of the C IV blueshift. The C IV blueshift is measured relative to the near-infrared ICA redshift.

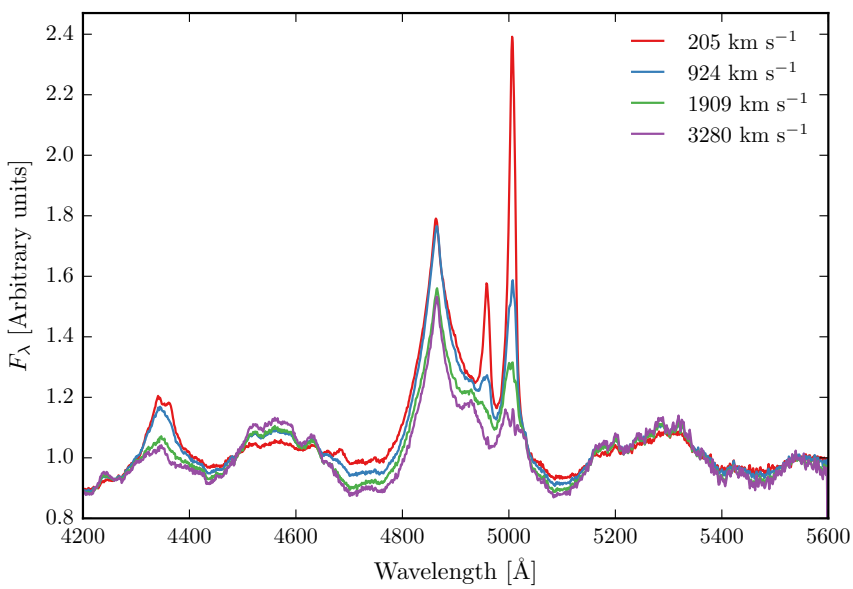

Figure 1.20: Median ICA-reconstructed spectra as a function of the C IV blueshift.

EV1 correlations

In Figure 1.19 we show how the [O III] strength varies as a function of the C IV blueshift. There is a very well defined relation: when C IV is strongly blueshifted [O III] is very weak. This is very similar to what we found when we used Gaussian functions to model the emission. The correlation between C IV blueshift and [O III] EQW is shown in a different way in Figure 1.20. Here we divide our sample into four bins according to the C IV blueshift. From the quasars in each C IV blueshift bin we then find then generate an ICA spectrum using the median weights from each quasar. The differences in the spectra as a function of the C IV blueshift are dramatic. [O III] becomes progressively weaker and more blueshifted. The anti-correlation with Fe III and the blue-ward Fe II also clear, but there is no change in the redward Fe II.

Updating EV1

The ICA can be thought of as update on EV1. EV1 is a quest for HR diagram for quasars - clearly very important. The spectral diversity is encapsulated in the EV1 components. Most of the variance in EV1 is the anti-correlation between the strengths of [O III] and Fe II. So at one end we have objects with strong Fe II and weak [O III], and at the other end objects with weak Fe II and strong [O III]. Other properties, including the C IV blueshift and the Hβ FWHM, also change systematically. Our work shows that the ICA component weights change systematically along the EV1 sequence.

Just present this as an idea for future work right at the end rather than having this sandwiched in the middle.

Accurate systemic redshift estimates are essential in a number of applications, and researchers have devoted a large amount of telescope time to obtaining near-infrared spectra to access [O III] for this purpose. HI, CO and absorption line measures of the host galaxy rest frame suggest that [O III] usually gives consistent results within 200 km s^{-1}(de Robertis 1985; Whittle 1985; Wilson & Heckman 1985; Condon et al. 1985; Stripe 1990; Alloin et al. 1992; Evans et al. 2001). However, our work shows that at high luminosities this can result in large errors (profile can be dominated by blueshifted component, Fe II emission can be improperly subtracted, or [O III] might not be detected at all. [O III] is weaker and broader so it is more difficult to detect and measure [O III] accurately for these luminous quasars (to for instance obtain reliable redshift estimates based on [O III])

1.8.5 *Future work*

Pros:

It is less sensitive to the spectral S/N, and the component weights do not need to be constrained. It is therefore much simpler to apply than fitting multiple Gaussians.

Cons:

The components were calculated using a set of lower-redshift, lower-luminosity AGN, and quasar spectra are known to vary systematically as a function of luminosity. For example, the [O III] line is typically broader in more luminous quasars. Because there are so few objects with very broad [O III] in the low-redshift sample, the ICA reconstruction fails to reproduce the broadest [O III] profiles in our sample.

Cross-talk between components.

The size of the narrow line region is roughly expected to scale as $L^{0.5}$ (e.g. Netzer et al., 2004). However, for high luminosity quasars with strong [O III] this gives NLR sizes which are unreasonably large (~100 kpc; Netzer et al., 2004).

See extra text from Brotherton paper. I could be confused here, but I think the Netzer argument goes that the nlr size increase with luminosity because there are more ionising photons. but then you run out of nlr to ionise. the luminosity of the quasar keeps increasing but the luminosity of the nlr flattens out. so the eqw starts to decrease. but we see a huge scatter in eqw at high luminosities. we can relate this to the C IV blueshift, which I don't think Netzer will have been able to.

We see a correlation between the [O III] velocity width and asymmetry. As the line gets broader it gets more blue-asymmetric. One interpretation of this is that the strength of the narrow core is decreasing, leading to a broader and more blueshifted profile (e.g. Shen and Ho, 2014).

[O III] is broader, which is consistent with these quasars having more massive BHs. [O III] also shows stronger blue asymmetries, suggesting that outflows are stronger/more prevalent at these higher luminosities/redshifts. The luminous blueshifted broad wing and the extremely broad profile reveals high-velocity outflowing ionized gas. Our results therefore suggest that kilo-parsec-scale outflows in ionized gas are common in this sample of high-luminosity, high-redshift quasars.

1.9 RADIO

Radio properties would be interesting. Have another look, and at least say we tried and there aren't enough objects.